Published in final edited form as:
J Mol Biol. 2014 November 11; 426(22): 3811–3826. doi:10.1016/j.jmb.2014.08.023.

Insights into the Mechanisms of Membrane Curvature and Vesicle Scission by the Small GTPase Sar1 in the Early Secretory Pathway

Hanaa Hariri[1], **Nilakshee Bhattacharya**[1], **Kerri Johnson**[2], **Alex J Noble**[3], and **Scott M. Stagg**[1,2,‡]

[1]Institute of Molecular Biophysics, Florida State University, Tallahassee, FL 32306.

[2]Department of Chemistry and Biochemistry, Florida State University, Tallahassee, FL 32306.

[3]Department of Physics, Florida State University, Tallahassee, FL 32306.

Abstract

The small GTPase protein Sar1 is known to be involved in both the initiation of COPII coated vesicle formation and scission of the nascent vesicle from the ER. The molecular details for the mechanism of membrane remodeling by Sar1 remain unresolved. Here we show that Sar1 transforms synthetic liposomes into structures of different morphologies including tubules and detached vesicles. We demonstrate that Sar1 alone is competent for vesicle scission in a manner that depends on the concentration of Sar1 molecules occupying the membrane. Sar1 molecules align on low curvature membranes to form an extended lattice. The continuity of this lattice breaks down as the curvature locally increases. The smallest repeating unit constituting the ordered lattice is a Sar1 dimer. The three dimensional structure of the Sar1 lattice was reconstructed by substituting spherical liposomes with galactoceramide lipid tubules of homogeneous diameter. These data suggest that Sar1 dimerization is responsible for the formation of constrictive membrane curvature. We propose a model whereby Sar1 dimers assemble into ordered arrays to promote membrane constriction and COPII-directed vesicle scission.

Keywords

GTP hydrolysis; Sar1 lattice; dimerization; N-terminal helix; ADE model; membrane scission

‡**Corresponding author:**sstagg@fsu.edu phone: 850.645.7872 Institute of Molecular Biophysics; Florida State University. 91 Chieftan Way; Tallahassee, FL 32306 .
Hanaa Hariri: hhh09c@my.fsu.edu **Nilakshee Bhattacharya:** nb02c@fsu.edu **Kerri Johnson:** kmj09e@my.fsu.edu **Alex Noble:** ajn10d@fsu.edu

Introduction

In eukaryotic cells, early steps in the secretory pathway involve the formation of vesicles that traffic the newly synthesized proteins from the ER to the Golgi apparatus [1]. The biosynthesis of these vesicles depends on the ability of cells to deform membranous compartments. Several mechanisms of membrane remodeling rely on the interplay between proteins and membranes [2]. Scaffolding proteins that bind membranes directly or through linker proteins promote and stabilize membrane curvature through their charged and structurally curved domains [3]. Local membrane curvature can also be induced by the insertion of an amphipathic helix of proteins into the outer bilayer leaflet to create bilayer asymmetry [4,5]. Efficient membrane curvature is attained by the collaboration of several factors.

A set of five cytosolic proteins (Sar1, Sec23, Sec24, Sec13 and Sec31) constitute the “coat protein II” (COPII) coat machinery that transports nascent proteins from the ER to the Golgi [6]. The COPII components function synergistically to sculpt a highly curved bud on the ER membrane that eventually gets pinched off at the neck that connects it to the parent membrane. The small GTPase protein Sar1 is required for the formation of the COPII vesicle from the ER [7]. Upon exchanging GDP for GTP, Sar1 undergoes a conformational change that exposes an N-terminal amphipathic α-helix allowing it to insert into the outer membrane leaflet [4]. Sar1 directly interacts with Sec23 and thus recruits the Sec23/24 dimer which acts as a scaffolding complex that enhances membrane curvature through its membrane proximal concave surface [8]. At the later stages of assembly, the outer COPII coat component, the Sec13/31 complex, is recruited. Sec13/31 mediates COPII coat flexibility and plays a structural role in promoting the formation of coats of different geometries [9–11]. Finally, newly formed COPII-coated vesicles get pinched off from the ER and are shipped along with the encapsulated cargo to their target destinations [4,5].

The mechanism for COPII vesicle scission, particularly the role and relevance of GTP hydrolysis, remains elusive [12]. In previous studies, *in vitro* reconstitution reactions using a minimal set of yeast COPII proteins and liposomes have yielded COPII-coated vesicles [5,13]. Vesicle scission was thought to be achieved by the interplay between the COPII subunits and a functional Sar1 [13]. A previous study showed that Sar1 proteins that lack the N-terminal α-helix are incapable of vesicle separation despite normal recruitment of COPII components [5]. This evidence suggested that the N-terminal α-helix insertion is critical for promoting scission events. Further evidence suggested that an active Sar1 protein proceeds through GTP hydrolysis to constrict vesicle necks by disrupting local lipid packing leading to vesicle scission [4,5]. However, a more recent study demonstrated that COPII vesicle scission occurs independent of GTP hydrolysis by Sar1 [14]. Therefore, controversy still exists around the role of Sar1, GTP hydrolysis, and helix insertion in catalyzing membrane constriction and vesicle scission during COPII vesicle biogenesis.

Existing structural data has been useful to demonstrate the mechanism of GTP hydrolysis catalyzed by Sar1. Crystal structures exist for N-terminally truncated Sar1 bound to GDP (PDB: **1F6B**) and for Sar1 bound to GMPPNP (a non-hydrolyzable GTP analog) in complex with Sec23/24 (PDB: **1M2V**) [8,15]. Additionally, several studies have analyzed the

behavior of Sar1 in the presence of membranes. It has been shown that Sar1 deforms liposomes into a variety of different structures such as flexible tubules, multi-budded vesicles, and rigid tubes that exhibit an ordered arrangement of Sar1 molecules [16,17]. Straight and rigid membranous extensions were only observed under non-hydrolyzing conditions [16]. Thus, the ability of Sar1 to form tubular extensions of different morphologies is regulated by the nucleotide-bound state [12].

How this notion relates to the regulation of membrane constriction *in vivo* remains unclear. The different tubular structures observed *in vitro* were also observed in cell-based systems [18]. Long tubular elements that range in diameter between 40–80 nm have been previously observed extruding from the ER upon addition of Sar1 to permeabilized normal rat kidney (NRK) cells [18]. In addition, multi-budded vesicles resembling “beads-on-a-string” structures were observed in permeabilized mammalian cells upon incubation with a GTP-restricted form of Sar1 and cytosol [19]. Therefore, Sar1 has a capacity to modify membranes into a multitude of structures *in vitro* as well as *in vivo*. Which conditions might favor the formation of one tubular structure versus another remain to be investigated.

The organization of Sar1 molecules on membranes provides insights into the mechanism of Sar1-mediated membrane deformation. However, the structure of full length Sar1 in the presence of membranes is still unresolved. A previous study indicated that membrane-bound Sar1 assembles into ordered scaffolds that were thought to mediate membrane scission [17]. Like Sar1, the small GTPase Arf1 of the COPI transport system was found to promote vesicle formation and release [5,20,21]. Further analysis provided evidence that the dimerization of Arf1 plays a key role in mediating scission in the COPI system [21]. Similarly, membrane-bound Sar1 was shown to form higher molecular weight complexes [4,17]. Therefore, oligomerization of Sar1 on membranes may be required to induce membrane deformation and vesicle scission. In this study, we set out to characterize the structure of Sar1-GTP bound to membranes in order to gain better understanding of the biological activities of Sar1 in a near-native environment.

Results

Membrane deformation depends on the nucleotide state of Sar1

Giant unilamellar vesicles (GUVs) composed of neutral and negatively charged lipids were prepared by electroformation and used as donor membranes. Sar1 in different nucleotide states was then added to the GUVs. The structure of naked GUVs (Fig. 1A), which showed smooth (featureless) unilamellar vesicles of 3-8 μm diameter, contrasted sharply with that of Sar1-coated liposomes (Fig. 1B). A flotation assay based on density gradient centrifugation was used to assess the efficiency of binding of Sar1 to GUVs [22] (Fig. S1). Structural rearrangements of the GUVs upon Sar1 binding were visualized using transmission electron microscopy (TEM).

Negative stain TEM indicated that incubations of Sar1 with GUVs and GTP generated long and flexible tubes (Fig 1C). In contrast, incubations with non-hydrolyzable GTP analogues (GMPPNP and GMPPCP) resulted in a dominant population of multi-budded structures that

we refer to as pseudo-vesiculated tubes (Fig. 1C). This suggested that locking Sar1 in an active conformation enhances membrane constriction.

In order to further test this possibility, we used a GTPase-defective mutant version of Sar1 ($Sar1^{H79G}$) that is a "constitutively active" Sar1 mutant. His79 is located in the switch II region of Sar1 that plays an important role in GTP hydrolysis. H79G mutation suppresses the ability of Sar1 to hydrolyze GTP [17]. Incubations of $Sar1^{H79G}$ with either GTP or non-hydrolyzable GTP analogs (GMPPNP and GMPPCP) resulted in high populations of pseudo-vesiculated structures (Fig. 1D); similar to the morphology that was observed with wild type Sar1 and GMPPNP (Fig. 1C). Furthermore, we used an intrinsic tryptophan fluorescence assay to test the conformation of wild type Sar1 and $Sar1^{H79G}$ in response to the nucleotide state (Fig. S2). This showed that Sar1 undergoes a conformational change in the presence of GTP that is not seen under nonhydrolyzing conditions [with $Sar1^{H79G}$-GTP or Sar1-GMPPNP]. Furthermore, when the membrane binding activity of wtSar1-GTP is compared to $Sar1^{H79G}$-GTP, a substantial fraction of wtSar1-GTP remains in the bottom unbound fraction in a flotation assay while almost all of the $Sar1^{H79G}$ goes to the top, membrane-bound fraction (Fig. S1 B,C). Previous observations established that GTP hydrolysis by Sar1 causes the N-terminal helical domain to retract into a surface pocket permitting dissociation from the membrane [5]. In light of these observations, our data suggest that the suppression of GTP hydrolysis stabilizes Sar1-membrane association. Therefore, Sar1-GMPPNP and $Sar1^{H79G}$-GTP are more likely to remain bound to the membrane for a longer time than the wild type.

Our observations about the morphologies of Sar1 coated membranes were verified using cryogenic EM (cryoEM) which preserves samples in a near-native, hydrated state. Similar to the negative stain images, cryo-electron micrographs showed a mixture of morphologically heterogeneous tubes that can be classified into three categories: (1) flexible tubules (diameter < 60 nm), (2) rigid tubules (diameter > 60 nm), and (3) pseudo-vesiculated tubules (vesicles attached by narrow necks) (Fig. 1E). Sar1 tubules in vitreous ice displayed a wide diameter range between ~45 nm and up to 200 nm with a median diameter of 100 nm (Fig. 1F).

The wide morphological heterogeneity of Sar1-coated carriers may be attributed to variations in the local Sar1 concentration in the proximity of the substrate membranes. This explanation agrees with the area difference elasticity (ADE) model for membrane deformation induced by amphiphiles. According to the ADE model, increasing amphiphile concentration in the outer layer of the membrane bilayer induces destabilization of the inner layer [23,24]. This leads to bilayer asymmetry, which is accommodated by shape and elasticity changes, thus transforming spherical GUVs into elongated cylinders or tubules. In our study, the N-terminal amphipathic helix of Sar1 behaves analogously to the single chain amphiphiles examined by Inaoka and Yamazaki, 2007. Thus, regulation of Sar1 N-terminal helix concentration on donor membranes may play a role in dictating the shape and size of cargo carriers prior to COPII recruitment.

Sar1 Induces Vesicle Scission Independent from GTP Hydrolysis

According to the ADE model, expansion of the outer bilayer results in beaded tubes which consist of small vesicles connected by narrow necks; further addition of amphiphiles results in vesicle scission [23]. Based on this notion, increasing the local concentrations of Sar1 N-terminal helices may enhance the asymmetry between bilayer leaflets leading to vesicle scission by Sar1 independent from GTP hydrolysis. Therefore, we propose that during the final stages of bud formation the separation of vesicles from donor membranes is controlled by the percentage occupancy or the local concentration of Sar1 molecules on those membranes.

To test this hypothesis, we incubated GUVs with increasing concentrations of GTPase-defective Sar1^{H79G} and visualized the outcomes at different time points using negative stain TEM. Incubating GUVs with ~2-fold higher concentration of Sar1^{H79G} than was previously used for tubulation assays resulted in a dominant population of pseudo-vesiculated tubules after ~10 minutes of incubation in reactions containing either GTP or GMPPNP (Fig. 2A). After 2 hours of incubation, detached vesicles were observed in both reactions (Fig. 2B). Using cryoEM we verified that the newly generated small vesicles have a textured surface corresponding to the Sar1 coat (Fig. 2C). The cryoEM images also revealed that the GUVs were converted almost entirely to vesicles within 2 hours as neither GUVs nor tubules were observed in those samples. Sar1-coated vesicles were predominantly 50-60nm in diameter (Fig. 2D), which is close to the smaller end of the size range observed for COPII-coated vesicles. Finally, incubations of wild type Sar1 and GMPPNP similarly showed pseudo-vesiculated tubules after ~10 minutes and detached vesicles after 2 hours (Fig. 2E, 2F). These data demonstrate that Sar1 alone is capable of vesicle scission in a concentration-dependent manner that is independent of GTP hydrolysis. Interestingly, in the presence of GTP, wild type Sar1 transformed GUVs into long and flexible tubules instead of the dominant pseudo-vesiculated morphology observed under non-hydrolyzing conditions. After 2 hours of incubation, a small number of vesicles were also evident (Fig. 2E, 2F).

According the ADE model, beaded tubes which resemble the pseudo-vesiculated tubules observed in our study are precursors to vesicle scission. The observation that Sar1 only forms pseudo-vesiculated tubules in the presence of GMPPNP compared to Sar1^{H79G}, which forms pseudo-vesiculated tubules both in presence of GTP and GMPPNP suggests that the ability of Sar1 to hydrolyze GTP may lower the rate at which vesicles are formed. This further supports our hypothesis that states that higher concentrations of Sar1 on membranes, achieved here by locking Sar1 in an active state using a hydrolysis-defective Sar1 (Sar1^{H79G}) or a nonhydrolyzable nucleotide analogs, promotes bud formation and induces vesicle scission.

Since it is difficult to infer with certainty with TEM that increasing concentrations of Sar1 promotes vesicle scission, we verified our results using dynamic light scattering (DLS). Using DLS we monitored the intensity autocorrelation functions over a period of time. Faster decay rates of these functions correspond to shorter autocorrelation times and thus smaller particles. These data can be used to determine the rate of Sar1-mediated vesicle scission under different activation conditions. We observed a gradual decrease in the decay rate in conditions where Sar1 is locked in an active state [wtSar1-GMPPNP and Sar1^{H79G}]

(Fig. 3A,B,C). The decrease in the decay rate was less prominent in reactions containing Sar1 and GTP (Fig. 3D). No changes were observed in control reactions containing only GUVs (Fig S3). Thus, similarly, based on these results, blocking GTP hydrolysis (and thus increasing the amount of Sar1 on the membrane) seems to facilitate vesicle scission. This provides additional evidence that higher membrane occupancy by Sar1 is required for vesicle separation from donor membranes.

The detailed molecular mechanism of vesicle scission by Sar1 has yet to be fully explored. However, it is worth noting that with this concentration of Sar1, a large population of tubules displaying periodically twisted regions was observed. Detailed examination using electron tomography (ET) verified the twisted morphology (Fig. S4). This is similar to the previously reported GTP-dependent twisting activity of the dynamin coat that resulted in supercoiled tubules and generated longitudinal tension that led to membrane scission [25]. Therefore, the twisted morphology observed for Sar1 tubules could also provide a mechanism by which Sar1 coat can promote vesicle scission in a manner similar to dynamin.

Curvature-dependent Sar1 organization

To gain insights into the molecular mechanism of Sar1-mediated membrane remodeling, we set out to explore the structure of Sar1 molecules on lipid membranes. A previous study reported that Sar1 organizes on lipid membranes and forms ordered scaffolds which appear as regular bands that pass in and out of phase [17]. In our study, incubations of $Sar1^{H79G}$-GTP and GUVs has yielded similar results (Fig. 4A). These observations suggest a helical arrangement of Sar1 molecules on tubulated membranes. In addition, we detected some tubes with a continuous pattern of longitudinal striations that were parallel to the long axis of the tube. Those striations appeared exclusively on low curvature surfaces, including rigid tubes of large diameter (Fig. 4B). This suggested that Sar1 organization is dependent on the degree of membrane curvature.

Similar patterns of striations were observed on lipid tubules preserved in vitreous ice as were observed in negative stain (Fig. 4C, upper panel). The degree of ordering was assessed by Fourier transforming images of individual tubules and looking for layer lines and spots in the Fourier transforms. Ordered diffraction patterns were observed on tubules with diameters from approximately 100 nm to 200 nm (Fig. 4C, lower panel). In contrast, tubules that were approximately 60 nm in diameter or less did not exhibit an obvious diffraction pattern (Fig. 4C). Heterogeneity in the less than 60 nm tubules was confirmed by manually selecting segments of the smaller tubules and subjecting them to reference-free alignment and classification. This resulted in six different class averages which showed heterogeneity in tubes diameters and unevenly separated peripheral densities corresponding to Sar1 (Fig. S5). Nonetheless, longitudinal stripes were observed in the class averages indicating that Sar1 was only locally ordered. These data suggest that tubules of smaller diameter and thus higher curvature only support local and inconsistent ordering of Sar1 molecules.

Implications of Sar1 lattice formation in membrane constriction

We next attempted to determine the structure of the Sar1 scaffold bound to membranes. The heterogeneity of individual Sar1-coated tubules derived from GUVs presented a challenge

for image analysis and cryoEM 3D reconstructions. In order to overcome this challenge, we substituted spherical liposomes with mixtures of lipids containing the glycolipid galactosylceramide (GalCer) which is known to form bilayer tubules with uniform diameters. Previous studies have used GalCer tubules as substrates to promote the formation of helical protein assemblies and yielded reconstructions that approach atomic resolution [26,27].

Upon addition of Sar1, the majority of GalCer tubules (~70%) appeared to be Sar1-coated (Fig. S6). Different degrees of Sar1 coating were evident where some GalCer tubes appeared to be heavily coated compared to others where Sar1 was sparsely bound or not bound at all (naked tubes) (Fig. S6). For structural analysis, we manually picked overlapping segments of whole tubules from cryoEM images. Comparison of reference-free class averages of naked and coated tubules showed peripheral densities that correspond to the Sar1 coat (Fig. 5A). The size of the lobes correlates to the size of the Sar1 crystal structure as was verified by manual docking of a Sar1 crystal structure using Chimera (PDB: **2FMX**) [28,29] (Fig. 5B).

A small population of tubules (~10%) displayed additional morphologies including partitioned, multilayed, and doubled tubules (Fig. S6). The partitioned tubules, to our knowledge, had never been observed before, so we set out to determine what the partitions were. The partitioned tubules were only evident in incubations containing Sar1 indicating that the partitions are Sar1 dependent. Cryo-electron tomography demonstrated that the partitions constitute discs that span the whole interior of the GalCer tubules and are generally oriented perpendicular to the long axis of the tube (Fig. 5C, 5D). Reference-free class averages of the untilted data show that the partitions have a structure consistent with a bilayer (Fig. S6). Together these data suggest that the partitions are a modification of the inner bilayer leaflet which occurs to accommodate the expansion in the outer bilayer leaflet induced by Sar1 N-terminal α-helix insertion.

The addition of GalCer restricted the heterogeneity inherent in the GUV-derived Sar1 tubules by making the tubules straight with homogeneous diameter, and thus more accessible for 3D structure determination. We reasoned that the heavily coated GalCer tubules would have the largest regions of ordered Sar1. Therefore, we generated a stack of segments cut from manually picked, heavily coated Sar1-GalCer tubules. In order to assess the degree of ordering of the GalCer tubules, reference-free alignment and classification was performed on segments of the GalCer tubules [30,31]. This resulted in five class averages that were composed of ~2,000 segments each (Fig. 6A). The Sar1 density on the outer layer of the tubules appeared ordered and well defined in local regions in the class averages, but it was clear that the order did not extend over the entire segments. Furthermore, computed diffraction patterns of the class averages did not show layer lines or spots that would indicate ordered or helical Sar1 binding. Therefore, these data are in agreement with our previous observation that the extended Sar1 lattices do not form on highly curved membranes. Instead, it forms locally ordered patches of Sar1 arrays similar to those formed on tubulated GUVs (Fig 4A, S5).

Given that the GalCer tubules did not have helical symmetry, we performed an asymmetric reconstruction of the tubules. The naked tubules were also reconstructed as a negative control (Fig. 6B). Compared to the naked GalCer tubule reconstruction, the 3D reconstruction of Sar1-coated tubules displayed an additional layer that was clearly connected to the layer beneath it (Fig. 6C). This additional layer displayed peripheral stripes that appear to be regularly spaced on some areas of the tube and disordered on other areas as shown in a difference map (Fig. 6D). In general, those densities created a circumferential and longitudinal striped appearance that was similar to that observed on GUV-derived Sar1 tubules. The size of those densities matches the size of Sar1 molecules as showed by docking of the crystal structure of Sar1 (Fig. 6E).

In order to cross validate the tubule reconstruction, cryoET was performed on the GalCer tubes. Alignment of subvolumes picked from the circumference of 33 Sar1-coated GalCer tubes was performed, with the average of the aligned subvolumes shown in Figure S7A. The subvolume average clearly shows circumferential striations (Fig. S7A, bottom) similar to those observed in the tubule reconstruction from untilted data. Multivariate data analysis of the aligned subvolumes was performed, and the four most prominent eigenvolumes are shown in Figure S7B, aligned to the rotationally symmetrized average of a reconstituted tube (transparent). The first eigenvolume (gray) shows substantial, patternless variations in the outer Sar1 layer, consistent with the observation of low long-range order in the Sar1-coated GalCer tubes seen in the untilted data. The second and third eigenvolumes (yellow and teal) show slight variation in the diameter of the inner layer. The fourth eigenvolume (purple, inset) shows moderate variation in the density of the inner layer. Figure S7C shows a portion of a reconstituted tube superimposed onto the corresponding tomographic volume. The reconstituted tube corroborates our untilted reconstruction, and shows that Sar1 is only locally ordered on the GalCer tubes.

These data demonstrate that the highly curved membranes of GalCer tubules restrict the ability of Sar1 to form long-range ordered arrays. Therefore, we propose that Sar1 molecules form ordered lattices with long-range order exclusively on low curvature structures. In order to further test this notion, structural analysis of Sar1 assembly on low curvature surfaces such as 2D sheets or rigid tubules of large diameter was performed.

Sar1 forms a lattice of dimers on low curvature membranes

Given the inconsistent helical arrangement indicated by the Fourier transforms of the Sar1 tubules generated from GUVs, we reasoned that the tubules had areas of local order but the order broke down over long distances. To account for this, the centers of the tubules were boxed out, aligned and classified based on the assumption that the central region could be used to determine the structure of the Sar1 lattice (Fig. 7A). From cryoEM images, we extracted overlapping segments from the centers of the ~100 nm Sar1-coated tubules to create a stack of segments. This stack was then subjected to reference-free alignment and classification [30,31]. Two of the resulting reference-free class averages and their computed Fourier transforms appeared to be mirror images of one another suggesting that we classified the near and the far side of the tubules separately (Fig. 7B). This further supports our hypothesis that Sar1 is only locally ordered; if the Sar1 was helically ordered over the length

of a given tube, the front side would be superimposed on the backside and we would not have been able to classify them separately.

Sar1 ordered arrays on 2D lipid sheets were evident in some electron micrographs (Fig. 7C). The computed Fourier transform of one of the two reference-free class averages closely resembles that of the lattice formed by Sar1 on a 2D lipid sheet (Fig. 7B, 7C). This further supports the assertion that the two reference-free class averages obtained correspond to the two sides (near and far) of Sar1-coated tubules.

On the basis of our cryoEM data analysis, a 2D lattice could be established in the P222 space group with a Sar1 dimer in the asymmetric repeating unit (Fig. 7D). The crystal structure of the Sar1 dimer bound to GDP (PDB: **1F6B**) can be fit into the EM density in two possible scenarios (Fig 7E). The size of the densities observed in the reference-free class averages correlate well with the size of Sar1 molecules in the crystal structure.

Taken together, these data demonstrate that Sar1 forms ordered lattices on tubules of diameters larger than 60 nm and reveals that the asymmetric unit of the lattice consists of a Sar1 dimer. On rigid tubules of diameter smaller than 60 nm, Sar1 forms ordered arrays that exhibit long-range disorder. These data suggest that membrane-directed Sar1 dimerization may be a prerequisite for the formation of ordered arrays.

Discussion

In the current study we explored the mechanisms for Sar1-induced membrane curvature and vesicle scission in the absence of COPII proteins. Our results reveal that Sar1 is capable of pinching-off vesicles in a concentration dependent manner independent from GTP hydrolysis. Additionally, Sar1 was found to form an organized lattice on membranes of low curvature. The smallest unit of the Sar1 lattice was resolved to be a Sar1 dimer. The consistency of the ordered binding of Sar1 diminished over long distances on highly curved tubules. This correlation between Sar1 lattice formation and the degree of tubule constriction implicates Sar1 organization in regulating membrane constriction prior to scission events.

Vesicle scission by Sar1

Early observations indicated that the N-terminal helix of Sar1 is critical for COPII vesicle scission [5]. However, the mechanistic details underlying the final stages of vesicle scission remain unclear. Based on initial evidence, vesicle scission was thought to be dependent on GTP hydrolysis which resulted in the retraction of Sar1 N-terminal helices from the bilayer thus disrupting local lipid packing [16]. However, COPII vesicle budding from synthetic liposomes has also been reported to occur in the presence of non-hydrolyzable GTP analogs such as GMPPNP. *In vitro* vesicle scission with non-hydrolyzable GTP was regarded as a possible artifact induced by mechanical force applied during sample preparation [16] since restricting GTP hydrolysis has been previously shown to block cargo transport *in vivo* [32]. However, using procedures that did not employ any mechanical trituration steps, Adolf *et al.* presented evidence showing that GTP hydrolysis is not required for the release of COPII vesicle from semi-intact cell systems [14]. Therefore, an apparent discrepancy still exists in

the literature regarding the role and relevance of GTP hydrolysis and the specific mechanism by which Sar1 catalyzes vesicle scission.

It has been reported that the addition of the five core COPII components to liposomes in the presence of GTP is sufficient to generate coated vesicles *in vitro* [13]. Our results showed that Sar1 alone can deform liposomes into a range of morphologically distinct structures including rigid tubules, pseudo-vesiculated tubules, and detached vesicles. Pseudo-vesiculated tubules were more frequently observed in non-hydrolyzing conditions suggesting that these structures are caused by the suppression of GTP hydrolysis (Fig. 2). Here we report that increasing the concentration of Sar1 molecules occupying the membrane leads to the transformation of Sar1-coated pseudo-vesiculated tubules into detached vesicles independent from GTP hydrolysis (Fig. 2). We demonstrate that membrane deformation by Sar1 occurs at higher rates with nonhydrolyzable GMPPNP compared to GTP (Fig. 3). Similarly, in the presence of COPII proteins, pseudo-vesiculated structures were observed upon incubation of Sar1 with GMPPNP [5,16]. These multibudded tubules were observed less frequently under hydrolyzing conditions in incubations with Sar1-GTP and COPII [5]. Therefore, in line with what Lee *et al*. suggested [5], we propose that the persistence of Sar1 molecules on membranes may induce vesicle scission independent of GTP hydrolysis.

Area difference elasticity model (ADE)

Sar1 induces membrane deformation by selectively expanding the outer bilayer leaflet with respect to the inner one upon insertion of its N-terminal helix leading to bilayer asymmetry [4]. This asymmetry is translated initially by the tubulation of spherical liposomes into structures of various morphologies including rigid tubules and multibudded or pseudo-vesiculated tubules. What conditions favor the formation of one structure over the other was previously unexplored. Here we show that locking Sar1 in an active conformation, which may further concentrate Sar1 on membranes, favors the formation of pseudo-vesiculated tubules. Based on this observation, we propose that increasing the amount of membrane-bound Sar1 molecules enhances bilayer asymmetry leading to the formation of pseudo-vesiculated tubules that eventually result in fully detached vesicles. While the concentration of Sar1 at which vesiculation was observed exceeds physiological Sar1 concentrations, it is likely that in the cell the GEF Sec12 may function to locally concentrate Sar1 on the membrane at ER exit sites by constantly recharging it with GTP.

The morphological heterogeneity of tubulation outcomes observed with Sar1 can be interpreted by the area difference elasticity (ADE) model for membrane deformation. According to the ADE model, GUVs undergo a similar transformation upon increasing the concentration of membrane-bound single chain amphiphiles [23]. In the case of Sar1, insertion of the N-terminal amphipathic α-helix into the bilayer induces bilayer asymmetry that is amplified upon Sar1 oligomerization. This locally concentrated area of membrane deformation results in increased elastic stress on the inner leaflet that ultimately causes fragmentation of the deformed liposomes into smaller vesicles.

Sar1 helix insertion mechanism

Membrane deformation by Sar1 has been thought to be initiated by the insertion of the N-terminal helix into the outer bilayer leaflet leading to selective expansion of the outer leaflet relative to the inner one [4]. However, the efficiency of membrane deformation generated by the helix insertion mechanism depends, not only on the amount of helices inserted per unit area, but also on the size of the helix, their depth of penetration, and behavior in the membrane bilayer [33,34]. Recent models have predicted that the inserted helices must occupy 10–25% of the membrane surface area in order to generate efficient curvature [35]. For Sar1, we estimate the N-terminal helix (~8Å wide x20Å long≈1.6nm^2) to take up to ~25% of the volume of the protein body (2.47nm x2.47nm=6.1nm^2). Therefore, only when Sar1 is well packed and covers 100% of the membrane surface, does the helix occupy ~25% of the membrane surface area. Interestingly, a recent study that measured membrane rigidity predicted that human Sar1 molecules interact with one another at the level of the membrane and form stiff scaffolds of restricted mobility [36]. Our results experimentally substantiate this prediction. We observed that Sar1 is capable of assuming a high degree of packing on the membrane surface by the formation of an ordered Sar1 lattice (Fig. 4B, 7B). Therefore, based on these data we suggest that the helix insertion alone is insufficient to explain the role of Sar1 in the generation of curvature required for bud formation. Instead, Sar1-mediated curvature relies on the ability of Sar1 to oligomerize on the membrane and self-assemble into ordered lattices.

Sar1 lattice of dimers

In the presence of membranes, several lines of evidence indicate that Sar1 forms high molecular weight species [4,17]. Our results now reveal the structure of the membrane associated Sar1 lattice (Fig. 7B). Here, the smallest repeating unit of the Sar1 lattice is clearly revealed to be a Sar1 dimer. These data provide an indication that Sar1 dimerization may be required to form an ordered lattice on membrane surfaces. This would be similar to the role of the related small GTPase Arf1 involved in COPI vesicle formation [20,21].

At the molecular level, COPI-coated vesicles are generated as a result of the assembly of two cytoplasmic components: Arf1-GTPase and a coatomer complex of seven COP proteins. Beck et al revealed that a point mutation that results in the loss of Arf1 propensity to dimerize (Arf1-Y35A) blocks vesicle scission despite normal recruitment of COPI coatomer [21]. They propose a model whereby dimerization and binding to the coatomer stabilizes Arf1 at the neck of a growing bud. Additionally, the fact that Arf1 GTPase activating protein is excluded from the bud neck region further constrains Arf1 to areas of unfavorable curvature causing membrane separation and vesicle release [21,37]. This is in some ways comparable to our model where we propose that the ability of Sar1 to dimerize stabilizes membrane binding and lattice propagation on regions of positive and shallow curvature in the proximity of the budding neck, which, in turn, finalizes bud separation. Therefore, in both scenarios, dimerization may act as stabilizing factor for Arf1 and Sar1 on the membranes leading to scission of the growing bud.

Protein dimerization has been regarded as a means to promote curvature by a variety of other membrane-shaping proteins [38]. Endophilin is another example of an N-BAR

domain-containing protein that binds to dynamin and is implicated in clathrin-mediated endocytosis of synaptic vesicles. Endophilin binds to membranes using the helix insertion mechanism, and at the same time dimerization occurs to further stabilize the protein on the membrane before binding to dynamin. For Sar1, crystallographic results have suggested that the dimeric state is the functionally relevant state for membrane deformation activities [28]. In agreement with the previous study, a recent model was proposed whereby Sar1 dimerization modulates membrane stiffness by an amount proportional to the degree of membrane coverage by the Sar1 dimer [36]. Therefore, similar to other membrane-shaping proteins, dimerization of Sar1 may provide the mechanism underlying membrane deformation and scission during the formation COPII vesicles.

A model for COPII vesicle budding

At the subcellular level, a higher level of complexity governs membrane deformation and vesicle scission during COPII vesicle biogenesis. COPII bud formation is confined to specific sites known as ER exit sites (ERES) where the COPII proteins are concentrated [39]. Although the expression levels of Sar1 are not high enough to solely catalyze membrane transformations that lead to vesicle scission, the localization of the Sar1 guanine exchange factor, Sec12, to the ERES may function in increasing the local concentration of Sar1 at the sites of bud formation [40]. We propose a model whereby Sar1 initiates membrane deformation by forming local areas of curvature at exit sites. Then, Sec23/24 and Sec13/31 act to shape the local deformations into a coherent bud. Finally, we suggest that Sar1-GTP catalyzes scission by oligomerizing in the vicinity of the bud necks. Thus the different components of the COPII machinery work together to achieve full vesicle separation (Fig. 8).

Role of GTP hydrolysis

While GTP hydrolysis may not be a requirement for the final stages of vesicle release, it has been shown to play a key role in cargo sorting [41] and vesicle uncoating [42]. The Sec23 component of COPII is a GTPase-activating protein (GAP) for Sar1 GTPase, and Sec13-Sec31 further stimulates this GAP activity [42,43]. A recent study reported that a point mutation of Sec23 which enhanced the GTPase activity of Sar1 led to the selective block of ER export of procollagen [44]. This indicates that a longer stay of COPII proteins on the membrane is required to package bigger cargo suggesting that GTP hydrolysis is required for regulating the effective concentration of COPII proteins on the membranes. Therefore, in the context of the whole COPII machinery, the timing of GTP hydrolysis controls the kinetics of coat assembly during vesicle formation. This may be key for defining the dimensions of the COPII vesicle and for packaging of larger cargo such as procollagen [44]. Therefore, Sar1 acts as both a structural and functional component of the COPII machinery exerting two distinct functions: (1) initiating membrane bending and vesicle scission which is dependent on the ability of Sar1 to form structurally ordered scaffolds independent of GTP hydrolysis; (2) cargo sorting and coat disassembly which is dependent on GTP hydrolysis.

Summary

The mechanism of COPII-coated vesicle scission and the specific role of Sar1 in efficient vesicle release are poorly understood. Our structural investigation of Sar1 coats on different lipid substrates showed that the formation of an ordered Sar1 lattice is sensitive to membrane curvature. A continuous Sar1 lattice was only observed on membranes that have shallow curvature, such as large tubes (diameter between 60nm and 200nm) and 2D lipid sheets (Fig. 7). Higher curvature substrates, such as tubules of diameter between 25nm and 60nm and GalCer tubules, supported the formation of partial Sar1 arrays that were only locally ordered. These data suggest a function for Sar1 scaffolds in (1) initiating deformation of low curvature membranes during the early stages of bud formation, and (2) mediating vesicle scission at the highly constricted bud necks. Our model predicts that Sar1 facilitates scission by forming ordered arrays at the level of the bud neck on the parent membrane. Then the propagation of the Sar1 lattice would act to squeeze the bud neck ultimately facilitating scission.

Materials and Methods

Protein Expression and Purification

In this study we used human wild type (wt) Sar1b and hamster mutant Sar1^{H79G}. Hamster Sar1 shares 99% amino acid identity with human Sar1b. Both wtSar1b and Sar1^{H79G} were expressed in BL21 *Escherichia coli* (E. coli) cells from modified pET11d plasmid, giving the proteins an N-terminal His_6 tag. The hamster Sar1^{H79G} construct was provided as a kind gift from Dr. William E. Balch. The wtSar1b (GenBank accession number BC093034) was cloned into the same pET11d vector as the hamster Sar1 was. Sar1 proteins used in this study have successfully been expressed to high yields and extensively purified with FPLC using Ni-affinity tag purification followed by size-exclusion chromatography (SEC). Protein fractions were isolated and stored at −80°C until use.

Formation of GUVs

DOPC, DOPS and cholesterol were purchased from Avanti Polar Lipids, Inc. GUVs were formed by electroformation as described by Long et al., 2010. In brief, 10-20 μg of lipid mixtures composed of 55 mol% DOPC, 35 mol% DOPS, and 10 mol% cholesterol dissolved in chloroform were deposited on a conductive glass slide coated with a thin film of indium tin oxide (ITO). The conductive slide was placed in a desiccator and the lipid droplet was allowed to dry under vacuum for at least 2 hours to overnight. A spacer was placed on the glass slide and another ITO-coated slide was placed on the spacer to form a sealed chamber. Using a syringe, minimal salt buffer (MSB: 25mM Hepes-KOH, pH 7.2, and 1mM $Mg(OAc)_2$)) was injected into the chamber. The chamber was connected to a power supply and subjected to low-frequency voltage (10 Hz). The voltage was progressively increased by 0.3 V every 10 minutes from 0 V to 0.9 V and left at 0.9 V for 3 hours. Then the voltage was increased to 1.2 V for 0.5-1 hour. To detach the GUVs formed on the slide, the chamber was subjected to low-frequency voltage (4 Hz and 1.4 V) for one hour. GUVs were recovered by gentle pipetting using a syringe.

Flotation Assay

To test the effect of various incubation conditions on Sar1 binding to liposomes we used the flotation assay which was previously developed [22]. After incubation of wtSar1b or $Sar1^{H79G}$ with lipids, the incubation mixture was placed at the bottom of a sucrose gradient prepared in MSB (30%, 25%, 0% sucrose) and subjected to 90 minutes centrifugation at 45,000 rpm in a TLS-55 rotor. Fractions were collected starting from the bottom to the top of the gradient, followed by sodium dodecyl sulfate polyacrylamide gel electrophoresis (SDS-PAGE) and Coomassie or silver staining.

Formation of GalCer Tubules

D-galactosyl-β-1,1′N-nervonoyl-D-*erythro*-sphingosine (GalCer) was purchased from Avanti Polar Lipids, Inc. Lipid tubules were prepared by adding GalCer at 50 vol% to 2 mg/ml stock lipid mixture (55 mol% DOPC, 35 mol% DOPS and 10 mol% cholesterol). Chloroform in the mixture was dried under argon and rehydrated in MSB to a final concentration of ~0.8 mg/ml by vortexing for 1 minute. The quality of tubules formed was assessed by TEM and stored at 4°C for no longer than one week.

Tubulation and Vesiculation

For tubulation experiments, wtSar1b or $Sar1^{H79G}$ was incubated with liposomes in MSB at 32°C for 2 hours. Reaction mixtures contained ~40 ng/μl GUV, 1.5 mM GTP, and 7 μM Sar1. Titrations with increasing concentrations of Sar1 and GTP were performed to determine conditions for vesiculation.

Dynamic Light Scattering

All measurements were performed using DynaPro instrument equipped with a temperature controlled micro-sampler. To an 80 μl GUVs solution in MSB, 14 μM Sar1 and 2 mM nucleotide (GTP or GMPPNP) was added to get a final volume of ~ 100 μl. After equilibration at 32 °C, 20 autocorrelation functions of the scattered light were measured with 20 acquisitions per measurement, each acquisition for 20 seconds. Autocorrelation data was analyzed using Dynamics 7 software.

Negative Staining Electron Microscopy

Sar1-coated tubes were prepared as described above. Carbon-coated copper grids were glow-discharged for 8-10 seconds using a Gatan Solarus plasma cleaner (Gatan, Pleasanton, CA). The samples were adsorbed onto the grids for 1-2 minutes, washed with MSB, then stained with 2% uranyl acetate for 1-2 minutes and allowed to air dry before visualization using transmission electron microscopy (TEM).

Cryogenic Electron Microscopy

Samples for cryogenic EM (cryoEM) were prepared by rapid plunging into liquid ethane using FEI Vitrobot Mark IV at 100% humidity and 4°C. Samples were prepared on plasma cleaned C-flat CF-2/2–4C-50 holey carbon grids (Electron Microscopy Sciences). After incubation, 3-5 μl of the reaction mixture were applied to the grid, blotted for 2.5 s, and then the grid was plunged into liquid ethane. Grids were transferred under liquid nitrogen to a

Titan Krios (FEI) transmission electron microscope equipped with a Gatan Ultrascan 4096 × 4096 CCD camera. Data were collected using the Leginon package for automated cryoEM image acquisition [45,46]. CryoEM images for tubulated GUVs were collected at 120 keV at a magnification of 37,000x and a defocus of −5.0 μm. At this magnification, the pixel size at the specimen level is 2.23 Å. CryoEM images for Sar1-coated GalCer tubules were collected at 120KeV using the same software package at a magnification of 59,000 x, a dose of 14.8 $e^{-}/Å^{2}$ and a defocus of −1.97 μm. At this magnification, the pixel size at the specimen level is 1.5 Å.

Electron Tomography

The tomography application of Leginon was used to acquire the tilt series through a range of ±64° with an angular increment of 2°. Images in the tilt series were aligned by cross correlation in the PROTOMO software package [47]. Tomograms were reconstructed using weighted back projection.

Subvolume Averaging

Subvolume averaging was performed using Dynamo [48]. 33 straight tubes of diameter ~60 nm were chosen from 19 tomograms that had been aligned using Protomo [47]. From the 33 tubes, the center of each subvolume was identified by tracing the center of each tube and creating a filament mesh using dynamo_tomoview and dynamo_model_edit, respectively. 10,660 subvolumes of sidelength 84, pixelsize 3.5 Å/pixel, and with ~50% overlap with nearest neighbors were extracted from the 33 tubes. Eight alignment iterations were performed using Dynamo running in parallel on 12 Nvidia Tesla M2050 GPUs. Classification was performed on a random subset of 750 subvolumes using Dynamo. Of the 50 eigenvolumes generated, the first four were analyzed based on the prominence of their eigenvalues (117, 40, 29, 8) compared to the remaining eigenvalues (6 to 2), which trailed off into noise.

Image Processing

Preliminary processing, such as particle picking and contrast transfer function (CTF) estimation, was performed using Appion online processing tool [49]. Particles were picked manually along the length of the tubes using the helical picking option. The CTF was estimated using the ACE software package in Appion. Individual particles were CTF-corrected by phase flipping, and stacks of images created were aligned and classified using XMIPP reference-free maximum likelihood [30,31]. 3D reconstructions were calculated using *sshelix* which is an in-house software based on iterative helical real space reconstruction (IHRSR) [51].

Statistical Analysis

For Sar1-coated tubes derived from GUV, diameter distribution histograms were calculated based on manual measurements of the tubes diameters in the cryoEM dataset (Fig. 1F). Similarly, the diameter of Sar1-coated vesicles was measured manually to calculate the histogram distribution (Fig. 2D). Two diameter measurements were made for each vesicle and the average of the two measurements was used in the statistical representation. For Sar1-

coated GalCer tubules, the morphological heterogeneity distribution was deduced from the number of segments that constituted each of the corresponding class averages generated by computation compared to the total segments in the stack used for classification (Fig S6).

Tryptophan Fluorescence

GTPase activity assay similar to that previously described by Antonny et al., 2001 was used to monitor Sar1 conformation change over time. Tryptophan fluorescence was recorded at 340 nm upon excitation at 297.5 nm. Measurements were performed at 32 °C using CARY Eclipse Fluorescence Spectrophotometer. Sar1 was added to ~ 550 μl MSB to a final concentration of 1.5 μM. After 5 minutes, nucleotides were added to a final concentration of 60 μM.

Supplementary Material

Refer to Web version on PubMed Central for supplementary material.

Acknowledgments

The work was supported by a National Institutes of Health grant (GM086892) and an American Heart Association grant (#0835300N).

Abbreviations

ADE	area difference elasticity
CryoEM	cryogenic electron microscopy
ET	electron tomography
GalCer	galactoceramide
GUV	giant unilamellar vesicles
TEM	transmission electron microscopy
ER	endoplasmic reticulum

References

[1]. Palade G. Intracellular aspects of the process of protein synthesis. Science. 1975; 189:347–58. [PubMed: 1096303]

[2]. McMahon HT, Gallop JL. Membrane curvature and mechanisms of dynamic cell membrane remodelling. Nature. 2005; 438:590–6. [PubMed: 16319878]

[3]. Farsad K, Ringstad N, Takei K, Floyd SR, Rose K, De Camilli P. Generation of high curvature membranes mediated by direct endophilin bilayer interactions. J Cell Biol. 2001; 155:193–200. [PubMed: 11604418]

[4]. Bielli A, Haney CJ, Gabreski G, Watkins SC, Bannykh SI, Aridor M. Regulation of Sar1 NH2 terminus by GTP binding and hydrolysis promotes membrane deformation to control COPII vesicle fission. J Cell Biol. 2005; 171:919–24. [PubMed: 16344311]

[5]. Lee MC, Orci L, Hamamoto S, Futai E, Ravazzola M, Schekman R. Sar1p N-terminal helix initiates membrane curvature and completes the fission of a COPII vesicle. Cell. 2005; 122:605–17. [PubMed: 16122427]

[6]. Barlowe C, Orci L, Yeung T, Hosobuchi M, Hamamoto S, Salama N, et al. Copii - a Membrane Coat Formed by Sec Proteins That Drive Vesicle Budding from the Endoplasmic-Reticulum. Cell. 1994; 77:895–907. [PubMed: 8004676]

[7]. Barlowe C, d' Enfert C, Schekman R. Purification and characterization of SAR1p, a small GTP-binding protein required for transport vesicle formation from the endoplasmic reticulum. J Biol Chem. 1993; 268:873–9. [PubMed: 8419365]

[8]. Bi X, Corpina RA, Goldberg J. Structure of the Sec23/24-Sar1 pre-budding complex of the COPII vesicle coat. Nature. 2002; 419:271–7. [PubMed: 12239560]

[9]. Noble AJ, Zhang Q, O'Donnell J, Hariri H, Bhattacharya N, Marshall AG, et al. A pseudoatomic model of the COPII cage obtained from cryo-electron microscopy and mass spectrometry. Nat Struct Mol Biol. 2013; 20:167–73. [PubMed: 23262493]

[10]. Stagg SM, LaPointe P, Razvi A, Gurkan C, Potter CS, Carragher B, et al. Structural basis for cargo regulation of COPII coat assembly. Cell. 2008; 134:474–84. [PubMed: 18692470]

[11]. Zanetti G, Prinz S, Daum S, Meister A, Schekman R, Bacia K, et al. The structure of the COPII transport-vesicle coat assembled on membranes. Elife. 2013; 2:e00951. [PubMed: 24062940]

[12]. Daum S, Krüger D, Meister A, Auerswald J, Prinz S, Briggs JAG, et al. Insights from reconstitution reactions of COPII vesicle formation using pure components and low mechanical perturbation. Biol Chem. 2014; 395:801–12. [PubMed: 25003385]

[13]. Matsuoka K, Orci L, Amherdt M, Bednarek SY, Hamamoto S, Schekman R, et al. COPII-coated vesicle formation reconstituted with purified coat proteins and chemically defined liposomes. Cell. 1998; 93:263–75. [PubMed: 9568718]

[14]. Adolf F, Herrmann A, Hellwig A, Beck R, Brugger B, Wieland FT. Scission of COPI and COPII Vesicles Is Independent of GTP Hydrolysis. Traffic. 2013; 14:922–32. [PubMed: 23691917]

[15]. Huang M, Weissman JT, Beraud-Dufour S, Luan P, Wang C, Chen W, et al. Crystal structure of Sar1-GDP at 1.7 A resolution and the role of the NH2 terminus in ER export. J Cell Biol. 2001; 155:937–48. [PubMed: 11739406]

[16]. Bacia K, Futai E, Prinz S, Meister A, Daum S, Glatte D, et al. Multibudded tubules formed by COPII on artificial liposomes. Sci Rep. 2011; 1

[17]. Long KR, Yamamoto Y, Baker AL, Watkins SC, Coyne CB, Conway JF, et al. Sar1 assembly regulates membrane constriction and ER export. J Cell Biol. 2010; 190:115–28. [PubMed: 20624903]

[18]. Aridor M, Fish KN, Bannykh S, Weissman J, Roberts TH, Lippincott-Schwartz J, et al. The Sar1 GTPase coordinates biosynthetic cargo selection with endoplasmic reticulum export site assembly. J Cell Biol. 2001; 152:213–29. [PubMed: 11149932]

[19]. Bannykh SI, Rowe T, Balch WE. The organization of endoplasmic reticulum export complexes. J Cell Biol. 1996; 135:19–35. [PubMed: 8858160]

[20]. Beck R, Sun Z, Adolf F, Rutz C, Bassler J, Wild K, et al. Membrane curvature induced by Arf1-GTP is essential for vesicle formation. Proc Natl Acad Sci U A. 2008; 105:11731–6.

[21]. Beck R, Prinz S, Diestelkötter-Bachert P, Röhling S, Adolf F, Hoehner K, et al. Coatomer and dimeric ADP ribosylation factor 1 promote distinct steps in membrane scission. J Cell Biol. 2011; 194:765–77. [PubMed: 21893600]

[22]. Bigay J, Antonny B. Real-time assays for the assembly-disassembly cycle of COP coats on liposomes of defined size. Methods Enzym. 2005; 404:95–107.

[23]. Inaoka Y, Yamazaki M. Vesicle fission of giant unilamellar vesicles of liquid-ordered-phase membranes induced by amphiphiles with a single long hydrocarbon chain. Langmuir. 2007; 23:720–8. [PubMed: 17209626]

[24]. Miao L, Seifert U, Wortis M, Dobereiner HG. Budding transitions of fluid-bilayer vesicles: The effect of area-difference elasticity. Phys Rev E Stat Phys Plasmas Fluids Relat Interdiscip Top. 1994; 49:5389–407.

[25]. Roux A, Uyhazi K, Frost A, De Camilli P. GTP-dependent twisting of dynamin implicates constriction and tension in membrane fission. Nature. 2006; 441:528–31. [PubMed: 16648839]

[26]. Wilson-Kubalek EM, Brown RE, Celia H, Milligan RA. Lipid nanotubes as substrates for helical crystallization of macromolecules. Proc Natl Acad Sci U S A. 1998; 95:8040–5. [PubMed: 9653136]

[27]. Wilson-Kubalek EM, Chappie JS, Arthur CP. Helical Crystallization of Soluble and Membrane Binding Proteins. Methods Enzymol Vol 481 Cryo-Em Part - Sample Prep Data Collect. 2010; 481:45–62.

[28]. Rao Y, Bian C, Yuan C, Li Y, Chen L, Ye X, et al. An open conformation of switch I revealed by Sar1-GDP crystal structure at low Mg2+ Biochem Biophys Res Commun. 2006; 348:908–15. [PubMed: 16899220]

[29]. Goddard TD, Huang CC, Ferrin TE. Visualizing density maps with UCSF Chimera. J Struct Biol. 2007; 157:281–7. [PubMed: 16963278]

[30]. Scheres SHW, Valle M, Carazo JM. Fast maximum-likelihood refinement of electron microscopy images. Bioinformatics. 2005; 21:243–4.

[31]. Scheres SHW, Valle M, Nunez R, Sorzano COS, Marabini R, Herman GT, et al. Maximum-likelihood multi-reference refinement for electron microscopy images. J Mol Biol. 2005; 348:139–49. [PubMed: 15808859]

[32]. Aridor M, Bannykh SI, Rowe T, Balch WE. Sequential Coupling between Copii and Copi Vesicle Coats in Endoplasmic-Reticulum to Golgi Transport. J Cell Biol. 1995; 131:875–93. [PubMed: 7490291]

[33]. Blood PD, Swenson RD, Voth GA. Factors influencing local membrane curvature induction by N-BAR domains as revealed by molecular dynamics simulations. Biophys J. 2008; 95:1866–76. [PubMed: 18469070]

[34]. Campelo F, McMahon HT, Kozlov MM. The hydrophobic insertion mechanism of membrane curvature generation by proteins. Biophys J. 2008; 95:2325–39. [PubMed: 18515373]

[35]. Stachowiak JC, Schmid EM, Ryan CJ, Ann HS, Sasaki DY, Sherman MB, et al. Membrane bending by protein-protein crowding. Nat Cell Biol. 2012; 14:944–9. [PubMed: 22902598]

[36]. Loftus AF, Hsieh VL, Parthasarathy R. Modulation of membrane rigidity by the human vesicle trafficking proteins Sar1A and Sar1B. Biochem Biophys Res Commun. 2012; 426:585–9. [PubMed: 22974979]

[37]. Bigay J, Gounon P, Robineau S, Antonny B. Lipid packing sensed by ArfGAP1 couples COPI coat disassembly to membrane bilayer curvature. Nature. 2003; 426:563–6. [PubMed: 14654841]

[38]. Gallop JL, Jao CC, Kent HM, Butler PJ, Evans PR, Langen R, et al. Mechanism of endophilin N-BAR domain-mediated membrane curvature. Embo J. 2006; 25:2898–910. [PubMed: 16763559]

[39]. Hong W, Tang BL. Protein trafficking along the exocytotic pathway. Bioessays. 1993; 15:231–8. [PubMed: 8517852]

[40]. Futai E, Hamamoto S, Orci L, Schekman R. GTP/GDP exchange by Sec12p enables COPII vesicle bud formation on synthetic liposomes. Embo J. 2004; 23:4146–55. [PubMed: 15457212]

[41]. Sato K, Nakano A. Dissection of COPII subunit-cargo assembly and disassembly kinetics during Sar1p-GTP hydrolysis. Nat Struct Mol Biol. 2005; 12:167–74. [PubMed: 15665868]

[42]. Antonny B, Madden D, Hamamoto S, Orci L, Schekman R. Dynamics of the COPII coat with GTP and stable analogues. Nat Cell Biol. 2001; 3:531–7. [PubMed: 11389436]

[43]. Yoshihisa T, Barlowe C, Schekman R. Requirement for a Gtpase-Activating Protein in Vesicle Budding from the Endoplasmic-Reticulum. Science. 1993; 259:1466–8. [PubMed: 8451644]

[44]. Kim SD, Pahuja KB, Ravazzola M, Yoon J, Boyadjiev SA, Hammamoto S, et al. SEC23-SEC31 the Interface Plays Critical Role for Export of Procollagen from the Endoplasmic Reticulum. J Biol Chem. 2012; 287:10134–44. [PubMed: 22298774]

[45]. Suloway C, Pulokas J, Fellmann D, Cheng A, Guerra F, Quispe J, et al. Automated molecular microscopy: The new Leginon system. J Struct Biol. 2005; 151:41–60. [PubMed: 15890530]

[46]. Suloway C, Shi J, Cheng A, Pulokas J, Carragher B, Potter CS, et al. Fully automated, sequential tilt-series acquisition with Leginon. J Struct Biol. 2009; 167:11–8. [PubMed: 19361558]

[47]. Winkler H, Taylor KA. Accurate marker-free alignment with simultaneous geometry determination and reconstruction of tilt series in electron tomography. Ultramicroscopy. 2006; 106:240–54. [PubMed: 16137829]

[48]. Castano-Diez D, Kudryashev M, Arheit M, Stahlberg H. Dynamo: A flexible, user-friendly development tool for subtomogram averaging of cryo-EM data in high-performance computing environments. J Struct Biol. 2012; 178:139–51. [PubMed: 22245546]

[49]. Lander GC, Stagg SM, Voss NR, Cheng A, Fellmann D, Pulokas J, et al. Appion: An integrated, database-driven pipeline to facilitate EM image processing. J Struct Biol. 2009; 166:95–102. [PubMed: 19263523]

[50]. Ludtke SJ, Baldwin PR, Chiu W. EMAN: Semiautomated software for high-resolution single-particle reconstructions. J Struct Biol. 1999; 128:82–97. [PubMed: 10600563]

[51]. Egelman EH. A robust algorithm for the reconstruction of helical filaments using single-particle methods. Ultramicroscopy. 2000; 85:225–34. [PubMed: 11125866]

HIGHLIGHTS

- Vesicle scission *in vitro* depends on the concentration of Sar1 at the surface of the membrane.
- Membrane deformation depends on the nucleotide state of Sar1.
- Sar1 forms an ordered lattice of Sar1 dimers.
- Assembly of the Sar1 lattice depends, in part, on the degree of surface curvature.

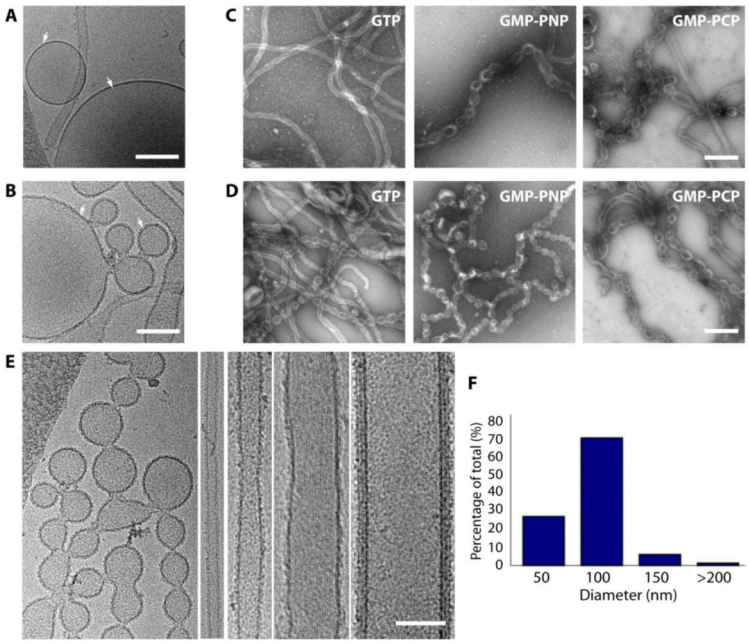

Figure 1. Sar1 transforms GUVs into tubular structures of heterogeneous morphologies

(A) Naked GUVs embedded in vitreous ice shows a smooth morphology compared to **(B)** the textured appearance of GUVs coated with Sar1 (arrows). Scale bar = 500 nm. **(C)** Human wild type Sar1 incubations with GUVs in presence of GTP, GMPPNP, and GMPPCP. Samples were adhered to glow-discharged EM grids and stained with 2% uranyl acetate (UAc) for imaging by EM. Scale bar = 200 nm. **(D)** Similar incubations were performed using GTPase-defective $Sar1^{H79G}$ mutant isoform. Scale bar = 200 nm. **(E)** CryoEM of tubular structures generated by $Sar1^{H79G}$ incubations with GUV and GTP. Scale bar = 100 nm. **(F)** Diameter distribution of $Sar1^{H79G}$ tubes determined from the cryoEM data.

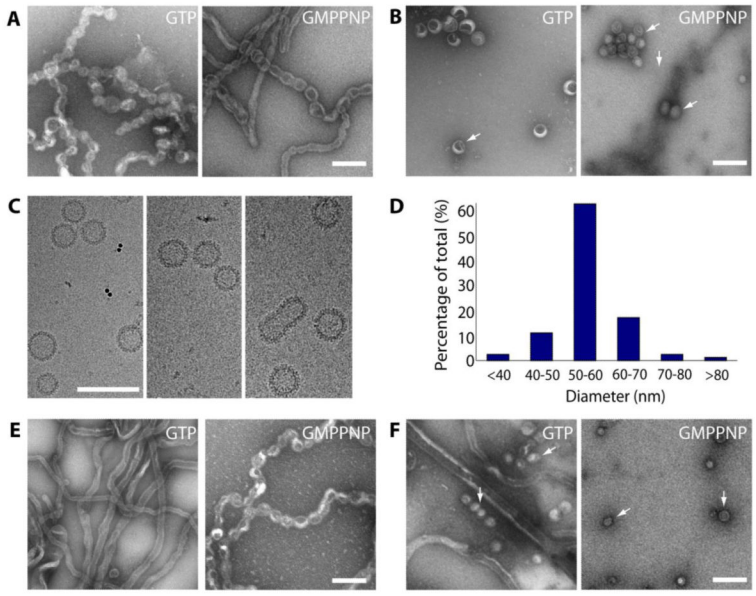

Figure 2. Formation of Sar1-coated vesicles

Incubations with increasing concentration of Sar1 was followed by staining with 2% UAc and EM imaging. **(A)** After 10 minutes of incubation of $Sar1^{H79G}$ with GTP and GMPPNP, pseudo-vesiculated tubes appear. Scale bar = 100nm. **(B)** After 2 hours of incubation smaller Sar1-coated vesicles appear in both conditions (white arrows). Scale bar = 100nm. **(C)** CryoEM of $Sar1^{H79G}$ -coated vesicles. Scale bar = 100nm. **(D)** Statistical analysis performed on the cryoEM vesicles data set. **(E)** Incubations with wild type Sar1 in presence of GTP and GMPPNP for 10 minutes. Scale bar = 100nm. **(F)** After 2 hours of incubation smaller Sar1-coated vesicles appear in both conditions (white arrows). Scale bar = 100nm.

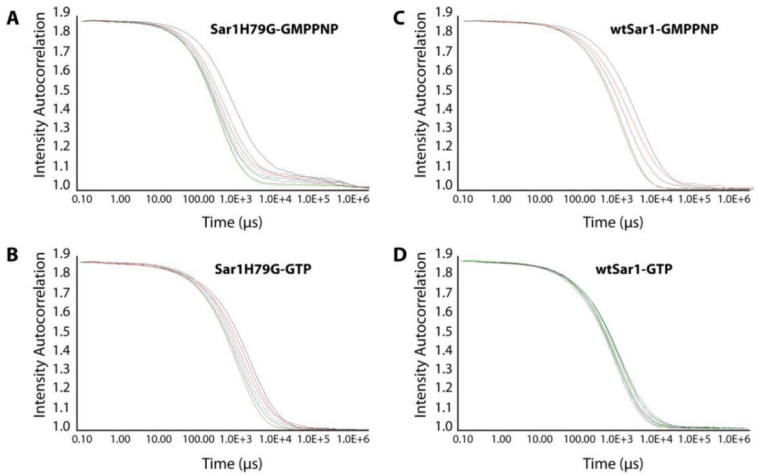

Figure 3. Dynamic light scattering on vesicle scission reactions

Incubations of Sar1^{H79G} or wtSar1 with GTP or GMPPNP were evaluated using DLS. Non-hydrolyzing conditions: **(A)** Sar1^{H79G}-GMPPNP, **(B)** Sar1^{H79G}-GTP, **(C)** Sar1-GMPPNP] show a prominent decay in the autocorrelation functions owing to the gradual decrease in the size of the outcome population. **(D)** The decay in autocorrelation functions was less prominent in Sar1-GTP incubations.

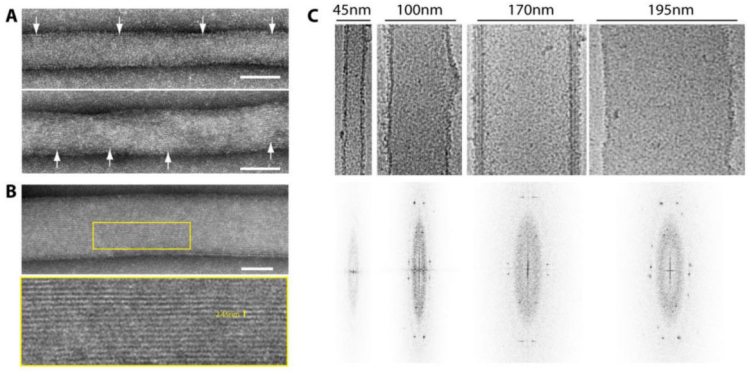

Figure 4. Formation of Sar1 ordered arrays on lipid tubules

(A) $Sar1^{H79G}$ -coated tubes of diameter < 60 nm show spaced striations indicative of inconsistent Sar1 ordering. Arrows point to repeated banding detected on tubule surfaces. Scale bar = 50 nm. **(B)** Tubes of diameter > 60 nm show continuous striations that are ~2.45 nm apart as shown after zooming in on the yellow tracing. Scale bar = 50 nm. **(C)** CryoEM of $Sar1^{H79G}$ -coated tubes (upper panel) and their corresponding calculated Fourier transforms (lower panel).

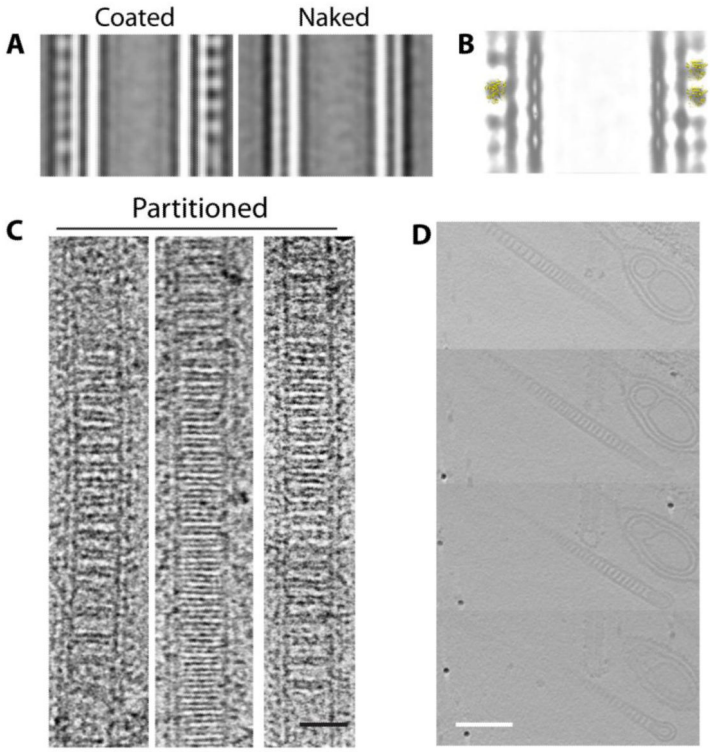

Figure 5. Sar1 ordered alignment is sensitive to membrane curvature

(A) Reference-free classification of naked and Sar1-coated GalCer tubes. **(B)** Fitting of Sar1 crystal structure (PDB: **1F6B**) into the density corresponding to the Sar1-coated class average. **(C)** Negative stain EM of partitioned tubes. Scale bar = 25 nm. **(D)** CryoET of the partitioned Sar1-GalCer tubes. Sections through the 3D tomogram showed partitions that appear as discs which span the whole interior of the tubes. Scale bar = 50 nm.

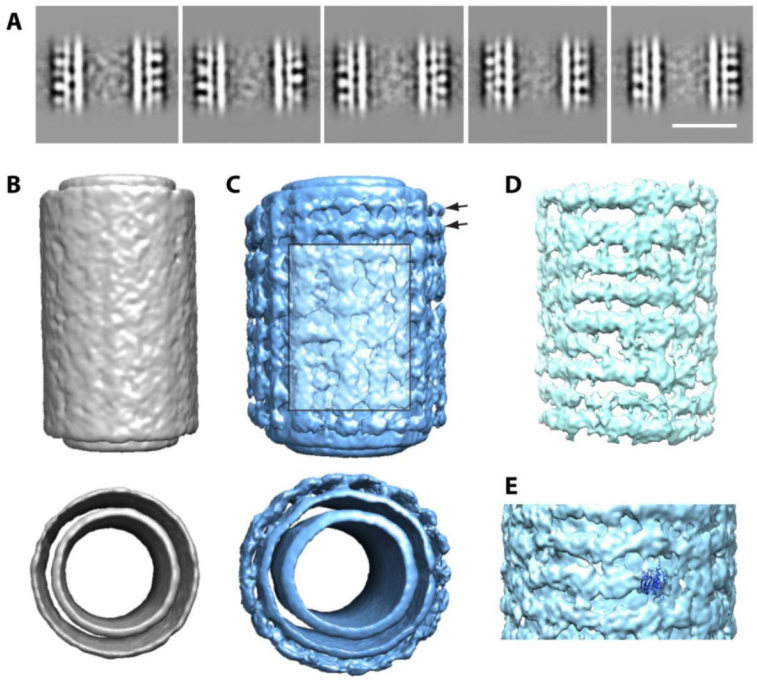

Figure 6. Sar1 forms locally ordered arrays on GalCer tubules

(A) Reference-free classification of heavily coated tubes. Scale bar = 25 nm. **(B)** 3D reconstruction of naked GalCer tubes (side and top views are shown). **(C)** 3D reconstruction Sar1-coated GalCer tubes (side and top views are shown). Arrows point to area of ordered striations. Boxed area of lighter color shows local disordered Sar1 binding. **(D)** Front section of the difference map between naked and Sar1-coated GalCer tubes showing horizontal Sar1 straitions. **(E)** Fitting Sar1 crystal structure (PDB: **1F6B**) into the 3D EM density of coated GalCer tubes.

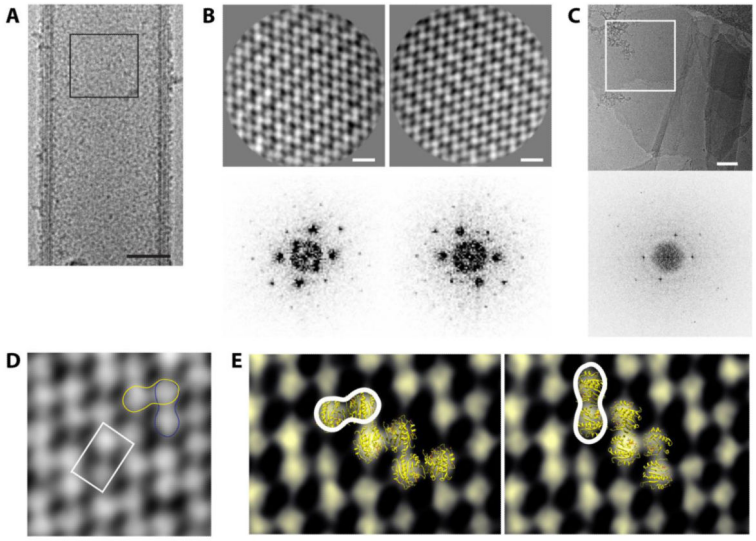

Figure 7. Ordered Sar1 arrays are composed of Sar1 dimers

(A) The middle regions of thick/rigid tubes of similar diameters (~ 100 nm) were segmented to create a stack which was used for further averaging and classification. **(B)** Reference-free class averages (upper panel). Scale bar = 5 nm. Lower panel shows the computed Fourier transforms. **(C)** CryoEM of 2D lipid sheets coated with Sar1 (upper panel). Scale bar = 100 nm. FT of the area traced in white is shown (lower panel). **(D)** P222 space group represented on the 2D Sar1 lattice with the asymmetric repeating unit shown (white tracing). Yellow and blue tracings represent the regions that fit the Sar1 dimer. **(E)** Fitting of Sar1 dimer (PDB: **1F6B**) into the electron density. Sar1 dimer can be fit in two possible scenarios (right and left).

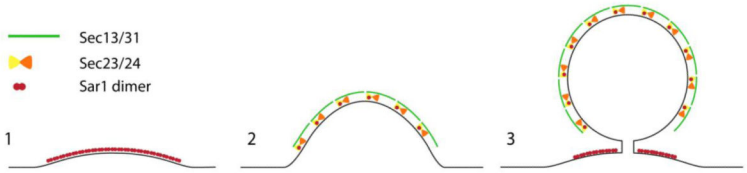

Figure 8. Depiction of a model for Sar1-mediated membrane deformation and vesicle scission

(1) Membrane-directed self-assembly of Sar1 into dimers drives the formation of an ordered lattice that initiates efficient membrane bending. **(2)** Increased membrane curvature triggers lattice dissociation. Recruitment of the remaining COPII components further enhances membrane bending and sculpting of a bud. **(3)** Sar1 lattice assembles at the level of the bud necks where curvature is relatively low. Propagation of Sar1 lattice assembly facilitates vesicle scission in coordination with the COPII coat.